ACS Catalysis

pubs.acs.org/acscatalysis Research Article

Tuning Strong Metal–Support Interactions via Synergistic Alloying

Jianyu Wang, Xiaobo Chen, Chaoran Li, Yaguang Zhu, Jing Li, Shiyao Shan, Adrian Hunt, Iradwikanari Waluyo, J. Anibal Boscoboinik, Chuan-Jian Zhong, and Guangwen Zhou*

Cite This: ACS Catal. 2024, 14, 5662–5674 Read Online

ACCESS | Metrics & More | Article Recommendations | Supporting Information

ABSTRACT: The encapsulation phenomenon associated with a strong metal–support interactions (SMSI) has been largely restricted to catalyst systems consisting of group VIII metals with high surface energy and reducible transition metal oxide supports with low surface energy. Here, we demonstrate an encapsulation phenomenon that, while sharing morphological similarities with conventional SMSI, follows a distinctive pathway. This is shown by the encapsulation of CuAu nanoparticles (NPs) supported on a highly ordered pyrolytic graphite (HOPG). Through dynamic monitoring of Cu, Au, and $Cu_{50}Au_{50}$ NPs in an oxidizing atmosphere using ambient-pressure X-ray photoelectron spectroscopy, we show that this spontaneous encapsulation is achieved through the synergistic effect of the alloying elements. Specifically, the surface segregation of Cu promotes dissociative O_2 adsorption, leading to the formation of atomic O species, while the subsurface enrichment of Au hinders O incorporation of oxygen into the bulk of CuAu NPs. Consequently, O spillover onto the graphite support occurs, resulting in the oxidation of the HOPG surface into graphitic oxide species. The higher affinity of the graphitic oxide species toward the Cu-segregated surface prompts their migration from the HOPG support to encapsulate the CuAu NPs. These results transcend the conventional SMSI and bear practical implications for the design and development of heterogeneous catalysts, particularly in carbon-supported alloy systems.

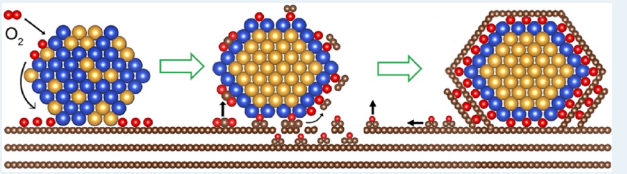

KEYWORDS: *strong metal–support interaction, nanoparticles, encapsulation, synergistic effect, copper–gold*

INTRODUCTION

Heterogeneous catalytic reactions are often carried out on supported metal nanoparticles (NPs) that are dispersed on a support to obtain and maintain a high metal dispersion and thus a stable high surface area. Supports are generally metal oxides or different forms of carbon materials able to anchor the active NPs and stabilize the catalyst against deactivation such as by leaching and sintering.[1,2] Oxide supports are known to interact with metals in complex ways to modify the catalytic properties of the system. One of the most well-known and important cases is strong metal–support interactions (SMSI) resulting from the encapsulation of the metal by a reduced thin oxide layer migrating from the oxide support during high-temperature treatment in a reducing atmosphere such as H_2.[3−7]

SMSI has been widely exploited to tune the catalytic performance of supported metals by engineering the geometric and electronic structures of the active metal sites for surface adsorption and dissociation of reactants. However, the SMSI state is largely restricted to a small number of catalyst systems that consist of group VIII metals with high surface energy and reducible transition metal oxides with low surface energy.[8] This specific combination of the metal and oxide support thereby provides the thermodynamic driving force for the spreading of the oxide species from the support onto the surface of the supported metals to lower the system energy. Consequently, it is extremely challenging for metals with a low surface energy (such as Au) to manifest SMSI due to the lack of sufficient driving force for the encapsulation.[9,10] Compared to the oxide-supported metals, it is also generally believed that carbon-supported metals are significantly less subjected to SMSI because of the much weaker interaction of the metal with carbon supports to result in an encapsulation layer.[11]

In contrast, herein, we report a completely different type of SMSI that results in the encapsulation of carbon-supported alloy NPs by a graphitic oxide layer that morphologically resembles the conventional SMSI but with a fundamentally different pathway leading to its formation. This is illustrated using ambient-pressure X-ray photoelectron spectroscopy (AP-XPS) and transmission electron microscopy (TEM) to monitor the dynamic interaction of CuAu NPs with carbon support, namely highly ordered pyrolytic graphite (HOPG) in O_2 gas, in contrast to the reducing atmosphere required for the conventional SMSI. Together with atomistic modeling, we show that this structural rearrangement of the alloy catalyst occurs as a result of the synergistic effect of the alloying

Received: December 19, 2023
Revised: March 18, 2024
Accepted: March 19, 2024
Published: March 30, 2024

https://doi.org/10.1021/acscatal.3c06171
ACS Catal. 2024, 14, 5662−5674

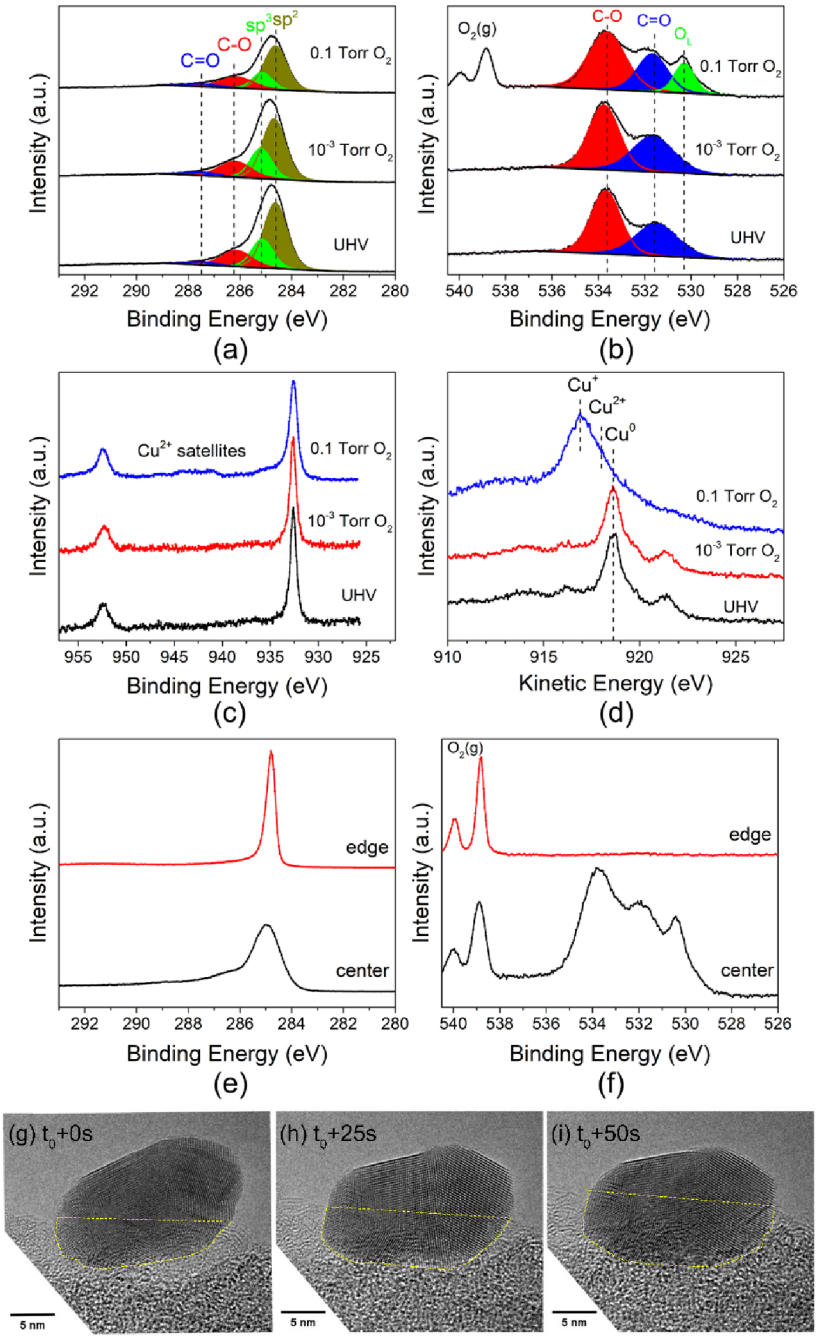

Figure 1. Evolution of photoelectron spectra obtained from HOPG-supported Cu NPs at 200 °C with the stepwise increase in pO_2 from UHV to 0.1 Torr. (a-d) C 1s, O 1s, Cu 2p, and Cu $L_3M_{45}M_{45}$ obtained from the center area of the HOPG covered by Cu NPs. (e, f) C 1s and O 1s obtained from both the center and outer edge regions of the HOPG at pO_2 = 0.1 Torr and 200 °C; the latter is free of Cu NPs. The doublet peaks from 538 to 541 eV in (b, f) are from gas-phase O_2. The XPS spectra are taken with a photon energy of 650 eV for C 1s and O 1s and of 1150 eV for Cu 2p and Cu LMM. (g-i) Time-lapse HRTEM images (Supplementary in situ TEM video 1) showing the gradual embedment of a Cu NP into the HOPG support during UHV annealing at 200 °C. The yellow dashed lines roughly delineate the region where embedment into the HOPG support occurs.

elements on driving the oxidation of the carbon support into the graphitic oxide that subsequently encapsulates the CuAu NPs. Our results on the scenario of engineering the nanoalloy provide opportunities to rationally maneuver the structure-dependent catalytic performance by circumventing the current limits in SMSI and expanding the boundaries of conventional SMSI to carbon-supported alloys, where carbon materials have been widely used for decades in heterogeneous catalysis as catalyst supports.

RESULTS AND DISCUSSION

As one of the model bimetallic systems, Cu−Au shows improved catalytic reactivity than the monometallic counterparts for various catalytic oxidation reactions including CO oxidation,[12,13] CO_2 reduction,[14,15] methanol synthesis,[16−18] and the water−gas shift reaction.[19,20] In this work, the dynamic evolution of Cu, Au, and $Cu_{50}Au_{50}$ NPs on the HOPG support is comparatively examined using in situ XPS and Auger electron spectroscopy (AES) to determine the effect of alloying

https://doi.org/10.1021/acscatal.3c06171
ACS Catal. 2024, 14, 5662−5674

on the encapsulation of the NPs in the O_2 atmosphere. The NP samples are synthesized by a wet chemistry approach[21,22] and are drop-cast onto the center region of the HOPG support for in situ AP-XPS measurements. Our in situ experiments start with annealing the NPs at 400 °C first in O_2 (1 Torr) to burn organic surfactants, then in H_2 (1 Torr) to reduce any metal oxide, and finally under ultrahigh vacuum (UHV), thereby obtaining a pristine state of the NPs before O_2 gas dosing at 200 °C. Real-time monitoring of the surface chemistry and composition evolution of the NPs is performed by acquiring XPS and AES spectra of C 1s, O 1s, Cu 2p, Au 4f, and Cu LMM in the presence of gas. To clearly elucidate the interactions between the NPs and the HOPG support, in situ XPS spectra are obtained from both the center and outer edge regions of the HOPG support, the latter of which is barely covered by NPs. Details of the material synthesis and in situ measurements can be found in the "Materials and Method" section.

Cu NPs on HOPG. HOPG-supported Cu NPs are exposed at 200 °C to O_2 stepwise in the O_2 gas pressure (pO_2). As shown in Figure 1a, the C 1s obtained from the pristine Cu NPs under UHV shows a broad peak that can be deconvoluted into four components with the binding energies (BE) of 284.8, 285.3, 286.3, and 287.6 eV, which correspond to the C−C bonds (sp^2) of perfect graphite, C−C (sp^3) bonds of defective graphite, C−O, and C═O bonds, respectively.[23−26] The C═O and C−O bonds should be located in the inner atomic layers of the HOPG support and cannot be removed by H_2 and UHV annealing. As illustrated in Figure 1a, the O_2 dosing results in the attenuation of the overall intensity in the C 1s region at higher pO_2 because of the scattering of the photoelectrons by gas molecules in the chamber. However, the C 1s spectral profile remains the same as that under UHV, including the BEs and the relative intensity ratio of the four C components, indicating that the HOPG support is unaffected from the exposure to the O_2 exposure.

Figure 1b shows the corresponding O 1s spectra from UHV annealing and subsequent exposure to the O_2 exposure. Consistent with the C 1s spectra, the O 1s obtained from UHV annealing consists of two major components with the BEs of 533.7 and 531.6 eV, which correspond to C−O and C═O,[27,28] respectively, in the subsurface of the HOPG. As the pO_2 increases to 0.1 Torr, a new peak appears at 530.4 eV, which corresponds to the lattice O in Cu_2O.[29] Gas-phase O_2 is also visible at 0.1 Torr, as shown by the doublet peaks from 538 to 541 eV. Figure 1c shows the corresponding Cu 2p, where the BE for Cu_2O is located at 932.6 eV. Weak satellite peaks are found at pO_2 = 0.1 Torr in 940−945 eV range, which are the characteristic feature of Cu^{2+} (CuO).[29] The kinetic energy of the corresponding Cu $L_3M_{45}M_{45}$ spectra (Figure 1d) shifts from 918.6 eV (metallic Cu under UHV) to 916.9 eV (Cu_2O) when pO_2 reaches 0.1 Torr with a shoulder at higher kinetic energy around 918 eV corresponding to CuO.[29] The combined O 1s, Cu 2p, and Cu LMM are mutually consistent and confirm that the Cu NPs are oxidized into Cu_2O with the presence of a small amount of CuO at pO_2 = 0.1 Torr.

The above XPS spectra are obtained from the center region of the HOPG support that has a high coverage of Cu NPs. For comparison, XPS spectra are also obtained at pO_2 = 0.1 Torr from the outer edge region of the HOPG that is barely covered by Cu NPs. As shown in Figure 1e, C 1s from the outer edge region has a highly symmetric line shape centered at 284.8 eV that corresponds to the C−C bonds (sp^2) of perfect graphite. In contrast, the C 1s obtained from the center region covered by Cu NPs has a much wider full width at half-maximum (fwhm) of the asymmetric line profile consisting of C−O, C═O, and defective graphite (sp^3) in addition to the perfect graphite component (Figure 1a). This is also consistent with the O 1s obtained from the two regions (Figure 1f), showing that the edge region is free of any peak intensity whereas the center region has strong intensity of the asymmetric line profile consisting of C−O, C═O, and lattice O (Figure 1b). The XPS results from the two regions indicate that Cu NPs can induce structure defects into the HOPG support during the thermal annealing, consistent with reported studies showing that metallic NPs can damage the surface layers of graphite.[30,31] This is further confirmed by our in situ TEM imaging (Figure 1g−i), which shows the gradual embedment of a Cu NP into the HOPG support due to its etching effect on the substrate during UHV annealing. The subsequent O_2 exposureleads to the diffusion of atomic O into the defective regions to form C−O and C═O bonds in the subsurface of the NP-covered region of the HOPG. By contrast, the bare HOPG region is relatively defect-free and highly inert toward O incorporation at the temperatures examined (up to 400 °C).

Au NPs on HOPG. Figure 2a,b shows C 1s, O 1s, and Au 4f spectra during the O_2 exposure of Au NPs on HOPG at 200 °C with the stepwise increase in pO_2 from UHV to 0.1 Torr. The Au NPs remain in the metallic state during the O_2 exposure, as confirmed by Au 4f that stays the same from UHV to the subsequent dosing of the O_2 (Figure 2b). As shown in Figure 2a, the C 1s obtained from UHV can still be deconvoluted into perfect graphite (C−C, sp^2), defective graphite (C−C, sp^3), C−O, and C═O, where the C−O and

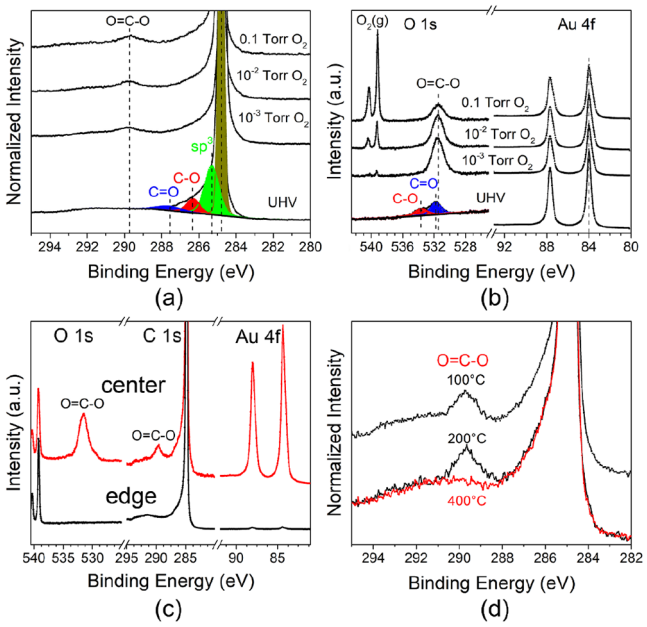

Figure 2. Evolution of photoelectron spectra obtained from HOPG-supported Au NPs at 200 °C with the stepwise increase in pO_2 from UHV to 0.1 Torr. (a) C 1s; (b) O 1s and Au 4f. (c) Au 4f, O 1s, and C 1s obtained from both the center and outer edge regions of the HOPG at pO_2 = 0.1 Torr and 200 °C. (d) Evolution of the C 1s from the center region (covered by Au NPs) of the HOPG by varying the temperature between 100 and 400 °C in 0.1 Torr O_2. The XPS spectra are taken with a photon energy of 650 eV for C 1s, O 1s, and Au 4f and a photon energy of 1150 eV for Cu 2p and Cu LMM.

https://doi.org/10.1021/acscatal.3c06171
ACS Catal. 2024, 14, 5662−5674

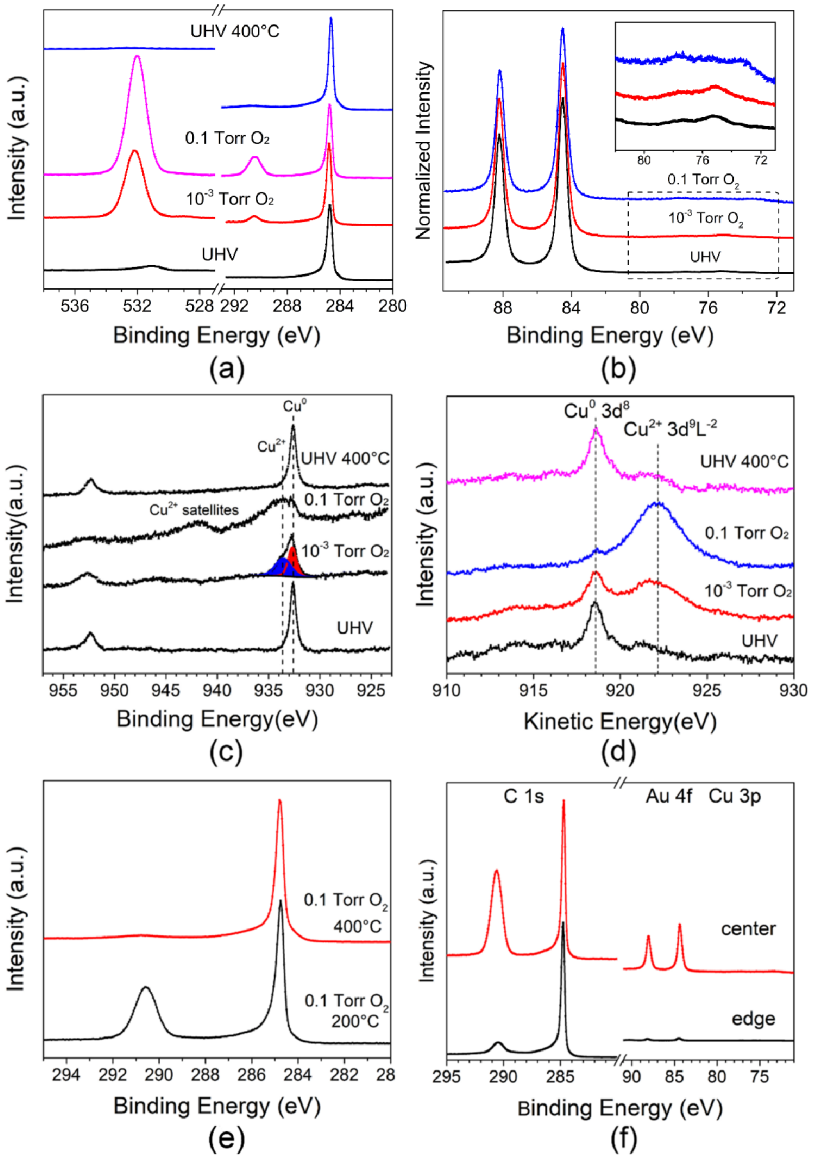

Figure 3. Evolution of photoelectron spectra obtained from the HOPG-supported $Cu_{50}Au_{50}$ NPs at 200 °C with the stepwise increase in pO_2 from UHV to 0.1 Torr. (a-d) O 1s, C 1s, Au 4f, Cu 3f, Cu 2p, and Cu LMM. The spectra at the top in (a, c, d) corresponds to UHV annealing at 400 °C after the O_2 dosing at 200 °C. The inset in (b) corresponds to the zoom-in view of the Cu 3f region. (e) Evolution of C 1s by swinging the temperature between 200 and 400 °C in 0.1 Torr O_2. (f) Au 4f and C 1s obtained from the center and outer edge regions of the HOPG support. The XPS spectra are taken with a photon energy of 650 eV for C 1s and O 1s and a photon energy of 1150 eV for Au 4f, Cu 3p, Cu 2p, and Cu LMM.

C═O components are from the initial O_2 annealing treatment to remove the surfactants. It can also be seen that the perfect graphite component has a much stronger peak intensity compared to that for the Cu NPs on HOPG (Figure 1a), indicating that the Au NPs have less of a damage effect on the HOPG support than the Cu NPs. Upon the O_2 exposure, a new peak emerges at 289.7 eV, which can be assigned to carbonate (CO_3^{2-}) or O═C−O in graphitic oxide.[23,32,33] Since Au maintains the metallic state during the O_2 dosing, this peak at 289.7 eV should be attributed to O═C−O due to the oxidation of the HOPG into the graphitic oxide. This is in contrast to the Cu NPs, where the HOPG support remains inert toward oxidation into graphitic oxide, as evidenced by the absence of this O═C−O peak during the O_2 dosing (Figure 1a). The C 1s spectra in Figure 2a are normalized with respect to the strongest peak of the perfect graphite component in order to verify any intensity changes of the other components. As shown in Figure 2a, the intensity of the O═C−O peak remains constant despite the increase in pO_2. This indicates that graphitic oxide formation is limited only to certain local areas of the HOPG support without further growth to cover a larger surface area.

Consistent with the evolution of C 1s, Figure 2b illustrates the corresponding O 1s and Au 4f spectra showing the presence of C−O and C═O peaks under UHV and the occurrence of the graphitic oxide peak (O═C−O) at 531.5 eV upon the O_2 dosing. It also shows that the C−O and C═O components disappear largely after the O_2 dosing, suggesting their further oxidation into graphitic oxide. The attenuated peak intensity of the O 1s at 0.1 Torr O_2 is due to the scattering of the photoelectrons by the gas molecules of higher pressure. However, it should be noted that the extent of

https://doi.org/10.1021/acscatal.3c06171
ACS Catal. 2024, 14, 5662−5674

intensity reduction differs between those of O 1 and Au 4f, which can be attributed to the kinetic energy of the photoelectrons. The binding energies for the photoelectron peaks of O 1s and Au 4f are ∼530 eV and ∼85 eV, respectively, corresponding to photoelectron kinetic energies of 120 and 445 eV for the XPS spectra taken with the incident photo energy of 650 eV in our experiments. Therefore, photoelectrons from the O 1s region, with lower kinetic energy, experience more attenuation due to gas molecule scattering compared with the photoelectrons from the Au 4f region.

Figure 2c shows the comparison of the spectra of O 1s, C 1s, and Au 4f obtained from the center region (covered by Au NPs) and the outer edge region (barely covered by Au NPs) of the HOPG support at pO_2 = 0.1 Torr and 200 °C. As can be seen, the intensity of Au 4f from the outer edge region is barely visible due to its extremely low coverage of Au NPs. More importantly, the graphitic oxide peak (O═C−O) is absent in both the C 1s and O 1s spectra obtained from the outer edge region. This confirms that the graphitic oxide formation is limited to the region that is in close proximity of the Au NPs. As shown later by DFT modeling, the interfacial perimeter of the Au NPs with the HOPG support is the location for stable O adsorption and thus oxidizing the graphite around the NP perimeter into the graphitic oxide. Figure 2d presents the C 1s spectra showing the intensity evolution of the graphitic oxide peak (O═C−O) by varying the temperature between 100 and 400 °C in 0.1 Torr O_2. As can be seen, the graphitic oxide peak disappears at ∼400 °C and reappears after lowering the temperature to ∼100 °C, as a result of the thermal decomposition of the graphitic oxide at the higher temperature and its reformation favored at the lower temperature. This is in good agreement with the other work showing the graphitic oxide decomposition over 325 °C.[34]

$Cu_{50}Au_{50}$ NPs on HOPG. Figure 3 illustrates the in situ XPS and AES measurements showing the evolution of HOPG-supported $Cu_{50}Au_{50}$ NPs at 200 °C with the stepwise increase in pO_2. As shown by C 1s in Figure 3a, the HOPG support under UHV is dominated by the highly ordered graphite component (C−C, sp^2) with BE = 284.8 eV. Upon O_2 exposure, a new peak emerges at BE = 290.4 eV, and its intensity increases with the increase in pO_2 from 1×10^{-3} Torr to 0.1 Torr. The C 1s peak at 290.4 eV is not reported in the literature. Consistent with the C 1s peak, a new peak at BE = 532.3 eV shows up in the corresponding O 1s region upon the O_2 dosing, and its intensity increases with increasing pO_2, as shown in Figure 3a. It should be noted that the peaks of chemisorbed O on Cu and lattice O in Cu oxides should be around 530 eV in the O 1s region.[29,35,36] The BEs of this component in the O_2 atmosphere are higher than that of the graphitic oxide (O═C−O) formed on the HOPG-supported Au NPs detected in both the C 1s region (BE = 289.7 eV) and the O 1s region (531.5 eV) (Figure 2a,b). Meanwhile, both the C 1s and O 1s peaks of this component on the HOPG-supported $Cu_{50}Au_{50}$ NPs have much stronger peak intensities than the peaks of the graphitic oxide on the HOPG-supported Au NPs under the same pO_2 condition, indicating its larger surface coverage on the HOPG-supported $Cu_{50}Au_{50}$ NPs.

Figure 3b illustrates the evolution of the Au 4f (90−82 eV) and Cu 3p (81−71 eV) regions upon exposure to O_2. Specifically, under UHV conditions, the Cu/Au intensity ratio is measured at 0.13. This ratio increases to 0.25 at 1×10^{-3} Torr O_2 and further increases to 0.36 at 0.1 Torr O_2, using the relative sensitivity factor (R.S.F.) values of 17.12 (Au) and 2.478 (Cu), respectively. The measurement indicates the surface segregation of Cu in $Cu_{50}Au_{50}$ NPs in the O_2 atmosphere, corresponding to the inward migration of surface Au into the bulk of the NPs.

Figure 3c shows the evolution of the corresponding Cu 2p spectra as a function of pO_2. Surprisingly, the satellite peaks at 940−945 eV and the shoulder peak at 933.5 eV, the typical characteristics of Cu^{2+}, appear at 1×10^{-3} Torr. The Cu^{2+}-like feature becomes more conspicuous at pO_2 = 0.1 Torr, as indicated by the strong satellite peaks and the strong peak at 933.5 eV. This is in contrast to the HOPG-supported Cu NPs, which are oxidized predominantly to Cu_2O at pO_2 = 0.1 Torr. This presence of the satellite peaks at 940−945 eV is coordinated with Cu LMM spectra in Figure 3d, showing a strong peak at 922.1 eV along with the weakened metallic Cu^0 peak at 918.6 eV at 0.1 Torr O_2. It should be noted that the kinetic energy (922.1 eV) of the strong Cu^{2+}-like peak in Figure 3d is much higher than the LMM peak (918 eV) for Cu^{2+} in CuO,[29] suggesting a different chemical state and surface structure for the HOPG-supported $Cu_{50}Au_{50}$ NPs. The LMM peak of Cu^{2+} in CuO is attributed to a $3d^8L^{-1}$ state, where L^{-1} indicates that there is one electron missing in the ligand valence state because the Coulomb interactions pull the 3d shell below the top of the O 2p band with a core hole due to photoexcitation.[37] By contrast, the kinetic energy of 922.1 eV observed from the $Cu_{50}Au_{50}$ NPs on HOPG arises from a final state that can be assigned to the $3d^9L^{-2}$ electron configuration. This happens as a result of the transfer of one extra electron from the bonded O−C═O group to the Cu atoms, leading to the $3d^9L^{-2}$ electron configuration when a core hole forms in Cu during photoexcitation. This photoemission process is similar to the CuO-like satellites in Cu 2p and Cu LMM induced by O chemisorption on Cu surfaces reported in the previous study.[37] Due to the electron loss, the oxidation state of the O−C═O group increases, resulting in higher binding energies of the C 1s (290.4 eV) and O 1s (532.3 eV) peaks for the $Cu_{50}Au_{50}$ NPs than the corresponding C 1s (289.7 eV) and O 1s (531.5 eV) peaks for Au NPs observed in Figure 2. More evidence exists to exclude the CuO formation as the origin of the satellite peaks in Cu 2p for the HOPG-supported $Cu_{50}Au_{50}$ NPs: (i) the BE for the O 1s peak in Figure 3b is much higher than that (530 eV) for the lattice O in CuO by 2.3 eV; (ii) CuO readily decomposes to Cu_2O under vacuum annealing at 400 °C;[38] by contrast, vacuum annealing of the $Cu_{50}Au_{50}$ NPs at 400 °C only results in a stronger metallic Cu^0 peak (along with the weakened Cu^{2+}-like LMM peak) without detecting the Cu_2O component (Figure 3d). Therefore, the Cu^{2+}-like LMM peak at 922.1 eV represents a specific chemical state of Cu that is directly bonded to the graphitic oxide to result in complex charge transfer between Cu and O−C═O. The higher kinetic energy of the Cu LMM peak at 922.1 eV and the higher BEs of C 1s at 290.4 eV and of O 1s at 532.3 eV are mutually consistent, pointing to the formation of a core−shell structure consisting of a graphitic oxide shell and a $Cu_{50}Au_{50}$ core. The formation of this graphitic oxide shell under an O_2 atmosphere is also consistent with the subsequent UHV annealing at 400 °C, for which the graphitic oxide shell becomes unstable and decomposes. This is evidenced by the disappearance of the O−C═O peak in C 1s and O 1s, the vanished satellite peaks in Cu 2p, and the shift of the Cu LMM peak from 922.1 eV (the Cu^{2+}-like feature) to 918.6 eV (metallic Cu^0) under UHV annealing at 400 °C, as shown in Figure 3a−d. Such thermal

https://doi.org/10.1021/acscatal.3c06171
ACS Catal. 2024, 14, 5662−5674

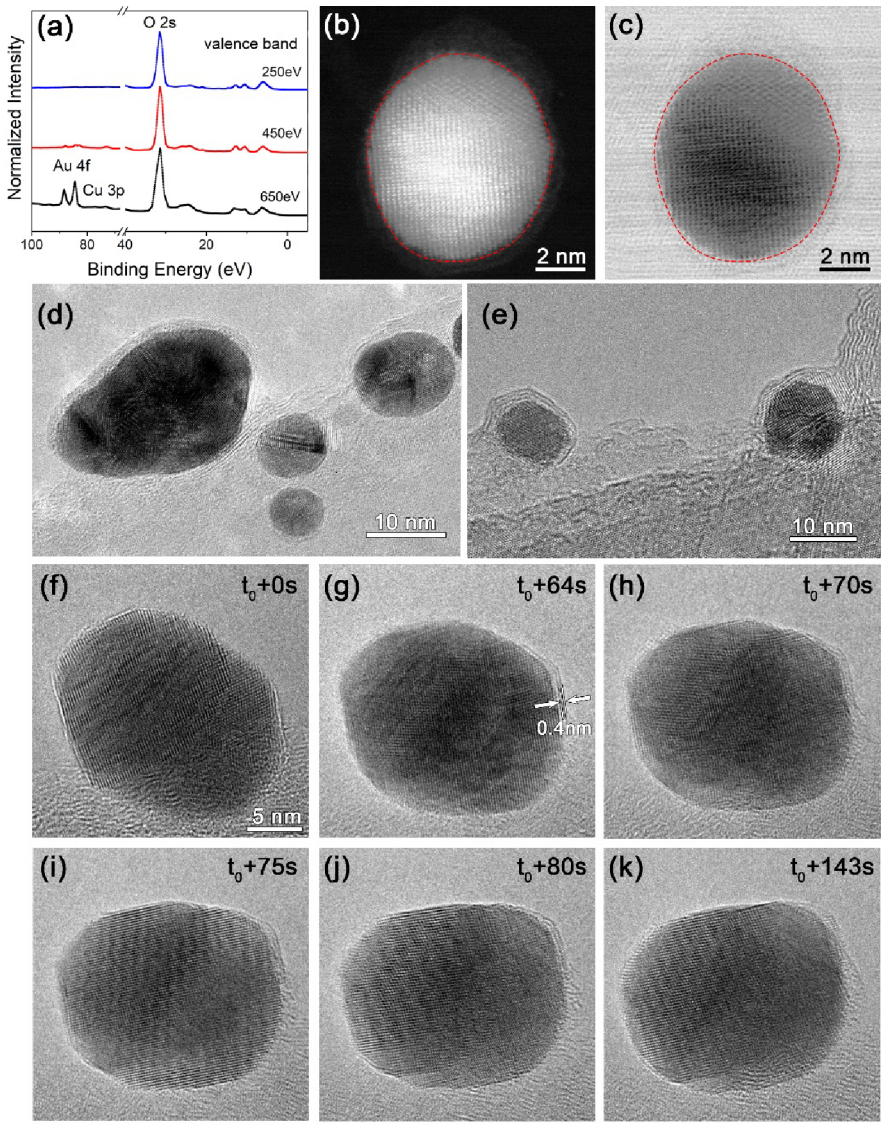

Figure 4. AP-XPS depth profiling analysis and in situ TEM imaging of the encapsulation of $Cu_{50}Au_{50}$ NPs by the graphitic oxide. (a) Au 4f, Cu 3p, and O 2s spectra of the HOPG-supported $Cu_{50}Au_{50}$ NPs measured with the photon energies of 250 eV, 450, and 600 eV, respectively, during the O_2 dosing at 200 °C and pO_2 = 0.1 Torr. The spectra are normalized to the maximum intensity of the O 2s peak. (b, c) Ex situ STEM HAADF and ABF images of a HOPG-supported $Cu_{50}Au_{50}$ NP after the O_2 annealing treatment. The dashed red and blue lines mark the $Cu_{50}Au_{50}$ core and the graphitic oxide shell, respectively. (d, e) Ex situ HRTEM images of the HOPG-supported $Cu_{50}Au_{50}$ NPs after the O_2 annealing treatment at 200 °C in a tube furnace. (f-k) Time-lapse HRTEM images (Supplementary in situ TEM video 2) showing the encapsulation of a $Cu_{50}Au_{50}$ NP loaded on the graphite support at 200 °C and 1×10^{-3} Torr of O_2 gas flow. t_0 represents the starting time of the image sequence.

annealing-induced decomposition of the graphitic oxide shell on the $Cu_{50}Au_{50}$ NPs is also consistent with the graphitic oxide formed along the interfacial perimeter of the HOPG-supported Au NPs (Figure 2d).

To further confirm this temperature-dependent evolution of the graphitic oxide shell, in situ XPS measurements are performed by swinging the temperature between 200 and 400 °C in 0.1 Torr O_2. As shown in Figure 3e, the O−C═O peak in C 1s disappears after raising the temperature to 400 °C and comes back after lowering the temperature to 200 °C, which not only confirms the preferential graphitic oxide formation at the lower temperature but also demonstrates the reversible encapsulation and de-encapsulation of the graphitic oxide overlayer by simply varying the reaction temperature. The effect of the $Cu_{50}Au_{50}$ NPs on the graphitic oxide shell formation is also confirmed by comparing the Au 4f and C 1s spectra obtained from the center region (covered by $Cu_{50}Au_{50}$ NPs) and the outer edge region (barely covered by $Cu_{50}Au_{50}$ NPs) of the HOPG support at pO_2 = 0.1 Torr and 200 °C. As shown in Figure 3f, the intensity of the graphitic oxide peak in C 1s is well correlated with the intensity of Au 4f, where the much weaker Au 4f from the outer edge region leads to a much weaker intensity of the O−C═O peak in C 1s. This further confirms the promoting effect of the $Cu_{50}Au_{50}$ NPs on graphitic oxide formation in their close proximity.

In addition to investigating the details of graphitic oxide formation on the HOPG-supported $Cu_{50}Au_{50}$ NPs, the resulting encapsulation of the $Cu_{50}Au_{50}$ NPs by the graphitic oxide is also probed by depth profiling using different photon energies of the incident X-rays. This is illustrated in Figure 4a, showing that the measurements with the higher photon energy of 650 eV yield stronger intensity ratios of the Au 4f and Cu 3p

https://doi.org/10.1021/acscatal.3c06171
ACS Catal. 2024, 14, 5662−5674

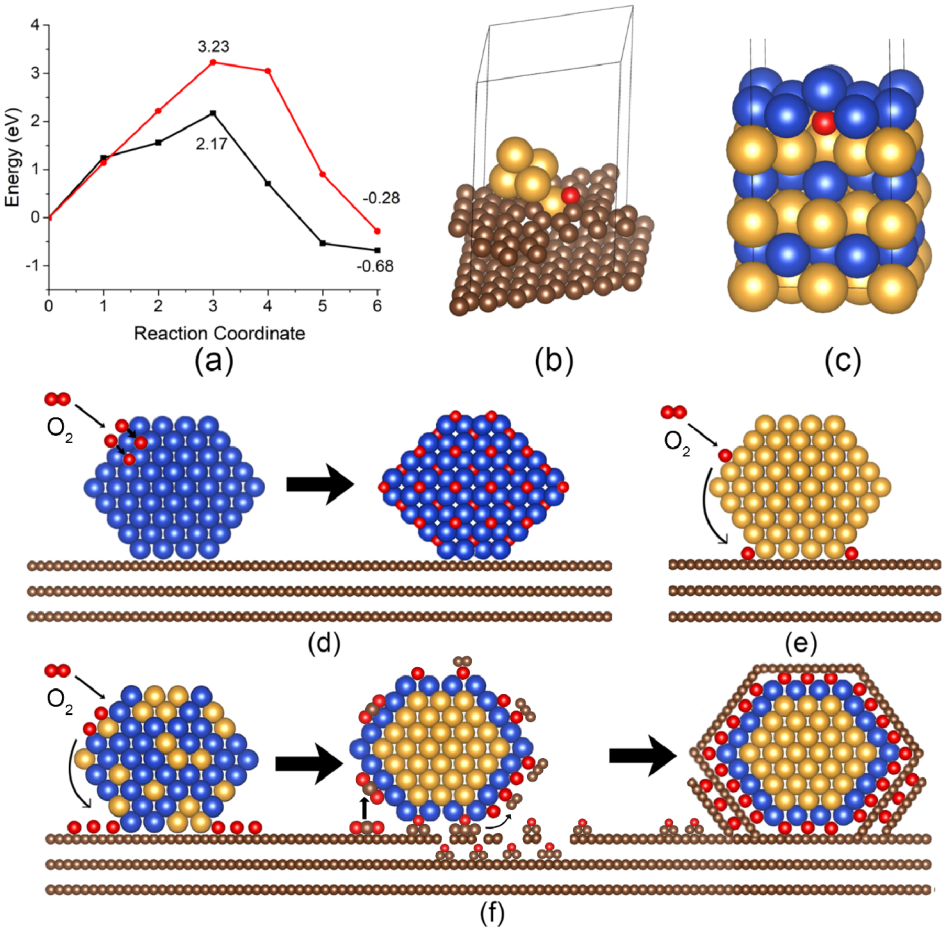

Figure 5. DFT modeling of dissociative adsorption of molecular O_2 on the HOPG-supported Cu, Au, and $Cu_{50}Au_{50}$ NPs. (a) Minimum energy reaction paths for the dissociation adsorption of molecular O_2 on Au(111) (black) and HOPG(0001) (red). (b) O adsorption along the interface periphery of an Au NP with the HOPG support. (c) O adsorption at the Au subsurface of the $Cu_{50}Au_{50}$ slab. (d-f) Pictorial illustration of the dynamic behavior of the HOPG-supported Cu, Au, and $Cu_{50}Au_{50}$ NPs in the O_2 atmosphere: dissociative O_2 adsorption results in complete oxidation of the Cu NP without spillover onto the HOPG; fewer O to oxidize the HOPG into graphitic oxide along the interface periphery between the Au NP and the HOPG support; spillover of a large number of atomic O from the Cu-segregated surface onto the surrounding HOPG to result in its oxidation into graphitic oxide species that undergo surface diffusion and evaporation to encapsulate the $Cu_{50}Au_{50}$ NP.

spectra with respect to O 2s compared with that by the photon energies of 450 and 250 eV. This is because the higher photon energy has the larger probing depth to reach the deeper region of the $Cu_{50}Au_{50}$ NPs underneath the graphitic oxide shell. Because the Au and Cu intensities can be detected with a photon energy of 650 eV but cannot be detected with a photon energy of 250 eV (Figure 4a), the thickness of the encapsulating layer should be limited to a few graphitic oxide layers.

This is corroborated well by ex situ scanning transmission electron microscopy (STEM) imaging of the HOPG-supported $Cu_{50}Au_{50}$ NPs after the AP-XPS measurements. Figure 4b illustrates a high-angle annular dark-field (HAADF) STEM image of such a $Cu_{50}Au_{50}$ NP, showing strong image intensities of Cu and Au atoms in the NP but much weaker intensity from the shell region due to the much lower atomic numbers of the graphitic oxide. Figure 4c is the complementary annular bright field (ABF) STEM image of the NP, in which the light element atomic columns in the graphitic oxide shell show up as a brighter image contrast. The atomically resolved STEM images also confirm the absence of any Cu oxides that would result in misfit dislocations due to the large lattice mismatch between the Cu oxides and the underlying $Cu_{50}Au_{50}$ alloy. To further validate the SMSI phenomenon, we conducted O_2 annealing of HOPG-supported $Cu_{50}Au_{50}$ NPs at 200 °C in a tube furnace. Figure 4d,e presents presentative HRTEM images of the $Cu_{50}Au_{50}$ NPs after the O_2 annealing treatment, showing that all the NPs are encapsulated with a few layers of graphitic oxide.

In situ environmental TEM imaging is employed to further confirm the encapsulation of the CuAu NPs by the graphitic oxide under the similar conditions as the AP-XPS experiments. This is performed by exposing the HOPG-supported CuAu NPs at 200 °C to ~1×10^{-3} Torr of O_2 while dynamically monitoring the NPs at the atomic scale. Figure 4d–i presents in situ HRTEM images showing the dynamic changes of a CuAu NP as it is seen edge-on. At the beginning of the in situ TEM image sequence, the NP is already covered partly with a single atomic layer of the graphitic oxide, as indicated by the red regions in Figure 4d. The trend for the surface encapsulation becomes more evident in Figure 4e–h, showing the upward spreading of the encapsulating layer from the corner region and its thickening to two atomic layers, where interlayer spacing is ~0.4 nm, larger than that (0.33 nm) for pristine graphite. The increased interlayer spacing suggests the partial oxygenation of the encapsulating graphitic oxide layer,

https://doi.org/10.1021/acscatal.3c06171
ACS Catal. 2024, 14, 5662–5674

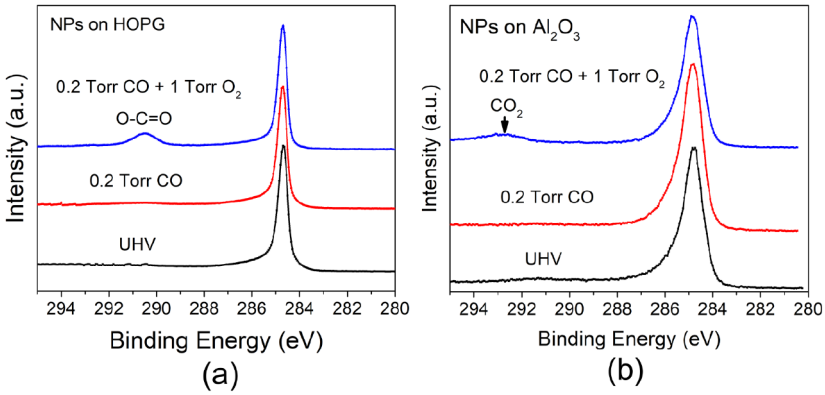

Figure 6. Catalytic performance of the CO oxidation at 200 °C under UHV, 0.2 Torr CO, and 0.2 Torr CO + 1 Torr O_2. (a) C 1s spectra obtained from the HOPG-supported $Cu_{50}Au_{50}$ NPs; (b) C 1s spectra obtained from the Al_2O_3-supported $Cu_{50}Au_{50}$ NPs.

agreeing with previous work of the increased interlayer spacing with increased oxidation extent of the graphitic oxide.[39] As noted in Figure 4k, the encapsulating graphitic oxide layer becomes thinner or disappears in some regions, which can be attributed to the electron beam-induced damage to the graphitic oxide layer, as confirmed from our in situ TEM imaging (Figure S1). The TEM imaging further corroborates the absence of any discernible Cu oxide formation, providing cross-validation to the AP-XPS results indicating the absence of CuAu oxidation into bulk oxides (Cu_2O and CuO) of Cu (Figure 3).

The results presented above highlight distinct behaviors of Cu, Au, and $Cu_{50}Au_{50}$ NPs on the HOPG support in the O_2 atmosphere. Specifically, Cu NPs undergo direct oxidation into Cu_2O and CuO, while Au NPs exhibit graphitic oxide formation solely along the interface periphery with the HOPG support. In contrast, $Cu_{50}Au_{50}$ NPs experience encapsulation by graphitic oxide. To shed light on the underlying mechanisms driving these differences, density functional theory (DFT) calculations are performed to examine the adsorption and dissociation of molecular O_2 on NPs, HOPG, and the interface periphery between NPs and the HOPG support. The DFT calculations focus on the (111) surface due to its lowest surface energy among the low-index surfaces of Cu and Au. For Cu NPs, O_2 molecules readily dissociate into atomic O, which strongly bonds with the Cu surface (adsorption energy: −1.67 eV; dissociation barrier of O_2: 0.23 eV), facilitating oxidation into Cu oxides (Figure S2). By contrast, O_2 dissociation on Au and HOPG surfaces encounters higher energy barriers with low probabilities (Figure 5a), and the interactions of the resulting atomic O with the Au and HOPG surface are repulsive (adsorption energies: + 0.21 eV for Au(111) and +1.08 eV for HOPG(0001)), consistent with prior work.[30,40] However, favorable O adsorption occurs along the interface periphery between Au NP and the HOPG support (adsorption energy: −0.78 eV; Figure 5b), leading to oxidation of C atoms near the interface periphery into graphitic oxide. This explains the limited graphitic oxide formation for the HOPG-supported Au NPs because of sufficient atomic O availability.

We now address the question of why the HOPG-supported $Cu_{50}Au_{50}$ NPs result in surface encapsulation of the NPs by the graphitic oxide. Initially, the surface of pristine $Cu_{50}Au_{50}$ NPs, following H_2 and UHV annealing treatment, is Au-rich and relatively inert toward dissociative O_2 adsorption. However, continued O_2 exposure drives the surface segregation of Cu atoms toward the surface, accompanied by the inward migration of surface Au atoms to the subsurface region (Figure 3b). This phenomenon aligns with previous work showing the switch in surface composition at $Cu_3Au(100)$ from an Au termination under UHV and H_2 conditions to a Cu termination in an O_2 atmosphere.[41] This Cu surface termination promotes dissociative O_2 adsorption, leading to the generation of a substantial quantity of atomic O. However, in $Cu_{50}Au_{50}$ NPs, the enrichment of Au in the subsurface region hinders the inward incorporation of atomic O into the NP bulk. This effect is confirmed by our DFT modeling, which reveals a positive adsorption energy (+0.57 eV) for the adsorption of the O in the subsurface region (Figure 5c). The presence of Au in the subsurface region creates a barrier that inhibits the diffusion of O into the NP bulk. Consequently, the surface properties and the O_2 adsorption behavior of $Cu_{50}Au_{50}$ NPs differ from those of pure Cu NPs due to the unique composition and structure of the alloy. As a result, the formation of Cu oxides within the $Cu_{50}Au_{50}$ NPs is not as prevalent as that in pure Cu NPs.

For the $Cu_{50}Au_{50}$ NPs, dissociative O_2 adsorption on the Cu-rich surface results in the spillover of a significant amount of atomic O onto the surrounding surface of the HOPG support. This leads to the oxidation of the defective graphite structure into a large number of highly mobile graphitic oxide species primarily due to their weak adhesion with the underlying graphite substrate. At elevated temperatures, these graphitic oxide species can undergo surface diffusion or even evaporation from the HOPG substrate and redeposit onto the $Cu_{50}Au_{50}$ NPs due to stronger interfacial adhesion. This phenomenon is supported by our DFT calculations, which show that the interface formed between Cu(111) and the O-adsorbed graphite layer has an adhesion energy of ~2.31 J/m^2, significantly stronger than the interlayer cleavage energy (0.38 J/m^2) of the graphite itself. This provides the strong driving force for the migration of the resultant graphitic oxide from the surrounding HOPG surface to encapsulate the $Cu_{50}Au_{50}$ NPs.

Figure 5d−f provides a schematic summary illustrating the key differences observed for Cu, Au, and $Cu_{50}Au_{50}$ NPs on HOPG as revealed through the in situ experiments and DFT modeling described above. For Cu NPs, dissociative O_2 adsorption results in a substantial generation of atomic O, directly oxidizing the Cu NPs into Cu oxides without spilling over onto the HOPG surface (Figure 5d). Once the Cu NP is fully oxidized, it loses activity for dissociative O_2 adsorption, leading to the termination of surface oxidation. In the case of

https://doi.org/10.1021/acscatal.3c06171
ACS Catal. 2024, 14, 5662−5674

the Au NP, dissociative O_2 adsorption occurs predominantly at the interface periphery between the Au NP and the HOPG support. This results in a limited amount of atomic O, which oxidizes the C atoms in the vicinity of the interface periphery into graphitic oxide species (Figure 5e). By contrast, surface segregation of Cu in $Cu_{50}Au_{50}$ NPs in the O_2 atmosphere enriches Cu at the surface, which in turn results in significant accumulation of Au in the subsurface and bulk due to their close proximity for small particle sizes. The Cu surface termination promotes the dissociation of O_2 into atomic O, which is more favorable to spill over onto the HOPG support than diffusing into the $Cu_{50}Au_{50}$ NP due to the low O affinity of the enriched Au in the subsurface and bulk. This results in the oxidation of the surrounding HOPG into graphitic oxide (CO_x) species by the atomic O. These CO_x species exhibit weak bonding with the HOPG substrate, allowing them to move freely across the surface or evaporate at elevated temperatures. In contrast, their stronger adhesion to $Cu_{50}Au_{50}$ compared to the weak physical van der Waals force with HOPG promotes their deposition onto the $Cu_{50}Au_{50}$. This results in surface encapsulation by single or multiple graphene oxide layers (Figure 5f). This process mirrors the oxidation of bulk graphite, which involves the multilayered aggregation of two-dimensional graphene oxide sheets.[42,43]

Lastly, we used the CO oxidation reaction ($CO + 1/2\ O_2 = CO_2$) to illustrate the important effect of graphitic oxide encapsulation on the catalytic performance of $Cu_{50}Au_{50}$ NPs. As shown in Figure 6a, initially, dosing 0.2 Torr CO over the HOPG-supported $Cu_{50}Au_{50}$ NPs at 200 °C does not induce noticeable changes in the C 1s region compared to that under the UHV. Subsequently, 1 Torr O_2 dosing is added into the XPS chamber to have a $CO:O_2$ ratio of 1:5. This results in the graphitic oxide encapsulation on the $Cu_{50}Au_{50}$ NPs, as evidenced by the detection of the O−C═O peak at BE = 290.4 eV. The absence of the gas-phase CO_2 peak (BE = 293.3 eV) indicates that graphitic oxide encapsulation deactivates the reactivity of the NPs toward CO oxidation. In comparison, $Cu_{50}Au_{50}$ NPs are loaded onto large Al_2O_3 particles, which are subsequently drop-cast onto the HOPG support. In this way, the $Cu_{50}Au_{50}$ NPs are separated from direct contact with the HOPG support, thereby suppressing the graphitic oxide encapsulation of the NPs. This is illustrated in Figure 6b, showing the absence of the graphitic oxide peak (O−C═O at BE = 290.4 eV) but the presence of the gas-phase CO_2 peak (293.3 eV) under 0.2 Torr CO + 1 Torr O_2 codosing. This comparison clearly demonstrates the detrimental effect of graphitic oxide encapsulation on the catalytic activity of $Cu_{50}Au_{50}$ NPs toward CO oxidation.

The concept of SMSI effects encompasses reversible encapsulation and de-encapsulation, offering a means to modulate the surface adsorption properties of heterogeneous catalysts.[44] Despite decades of research on constructing SMSI, this approach still faces significant limitations. First, the catalyst systems employed in this method are mostly restricted to reducible metal oxides combined with precious metals from the platinum group. Second, the formation of SMSI effects might coincide with the sintering of metal NPs because the treatment typically requires elevated temperatures exceeding 500 °C in H_2, leading to undesirable particle growth and agglomeration. In this work, we introduce a completely different pathway leading to encapsulation with a carbon support in O_2. Notably, the significantly lower temperature of 200 °C can largely suppress the metal NPs from sintering.

We anticipate that alloy NPs, such as Cu−Au, Cu−Pt, Ni−Au, Fe−Au, etc., comprising constituents with a significant discrepancy in chemical reactivity toward O, will exhibit a similar process to this SMSI phenomenon. This is because the oxidizing atmosphere can induce the surface segregation of the more reactive element (e.g., Cu, Ni, Fe, etc.) toward the surface, while enriching the more noble elements (Au, Pt) in the subsurface and bulk of the NPs. The enrichment of noble metals in the subsurface hinders the inward diffusion of dissociatively adsorded O, thereby promoting its spillover to the HOPG support. This results in surface oxidation of the surrounding HOPG support into graphitic oxide. Due to the weak adhesion between the graphitic oxide and the underlying graphite substrate, the graphitic oxide can undergo exfoliation from the HOPG substrate and migrate to encapsulate the NPs for stronger interfacial adhesion.

The potential practical implications of this type of SMSI resulting in graphene oxide encapsulation are multifaceted. First, the resulting graphitic oxide shells can serve as protective barriers for metal NPs and address the inherent issue of oxidation and degradation. Cu-based NPs are particularly susceptible to oxidation, but graphitic oxide encapsulation can effectively shield them from hazardous environments such as acid corrosion and oxidation, thus enhancing stability. Second, graphitic oxide encapsulation prevents the dissolution, disintegration, and aggregation, ensuring homogeneous dispersion of the NPs. While encapsulation may diminish the catalytic activity, as shown in Figure 6 with reduced activity toward CO oxidation, strategies such as chemical doping of the graphitic oxide framework can be employed to enhance surface reactivity. More importantly, our results demonstrate reversible encapsulation and de-encapsulation by simply changing the temperature in the same O_2 atmosphere. This allows for fine-tuning of the catalytic performance of the supported NPs by controlling the partial surface coverage of the graphitic oxide shell, achieving an optimal balance between the surface stability and reactivity.

Furthermore, controlling the alloy composition enables further control over the surface coverage of graphitic oxide on the NPs. This is evident from quantification of the intensities of the graphitic oxide peak (O═C−O) and the graphite peak (C−C, sp^2) shown in Figures 1−3. The ratios of graphitic oxide to HOPG are 0, ∼3.4%, and ∼12.9% for Cu, Au, and $Cu_{50}Au_{50}$ NPs, respectively, under 0.1 Torr O_2 annealing at 200 °C. This trend not only indicates the synergistic effect of Cu−Au alloying in promoting the encapsulation of the NPs by the graphitic oxide but also suggests the control of the degree of graphitic oxide encapsulation by controlling the Cu/Au composition. Specifically, a higher Au composition in the NPs favors higher coverage of the graphitic oxide shell.

CONCLUSIONS

This study presents an SMSI phenomenon involving HOPG-supported $Cu_{50}Au_{50}$ alloy NPs encapsulated by a graphite oxide layer. This encapsulation, resembling conventional SMSI morphologically, is formed through a fundamentally different pathway. Using a combination of AP-XPS, AES, and in situ TEM along with atomistic modeling, we monitor the dynamic interaction of Cu, Au, and $Cu_{50}Au_{50}$ NPs with the HOPG support in an O_2 gas environment. Our findings highlight the

https://doi.org/10.1021/acscatal.3c06171
ACS Catal. 2024, 14, 5662−5674

synergistic effect of the alloying elements on driving the oxidation of the HOPG support into graphitic oxide, leading to the encapsulation of $Cu_{50}Au_5$ NPs. Notably, this encapsulation adversely affects the catalytic activity of $Cu_{50}Au_{50}$ NPs with respect to CO oxidation. The incidence of this encapsulation are not observed in Cu and Au NPs. These findings expand the understanding of SMSI phenomena and offer possibilities for engineering nanoalloys to control catalytic performance by controlling the surface coverage of the graphitic oxide shell. The ability to manipulate alloy encapsulation on carbon supports may pave the way for designing and synthesizing other carbon-supported nanoalloys with tunable catalytic behavior, further enhancing the efficiency and selectivity of catalytic processes.

MATERIALS AND METHODS

Chemicals. Copper(II) chloride dihydrate ($CuCl_2{\cdot}2H_2O$ 99% pure) was obtained from Lancaster Synthesis. Hydrogen tetrachloroaurate (III) hydrate (HAuCl4) was obtained from Strem Chemicals. Tetra-*n*-octylammonium bromide (TOABr, 98%) was obtained from Alfa Aesar. 1-Decanethiol (96%), potassium bromide (99%), sodium borohydride (99%), hexane, toluene, and other common solvents used were obtained from Aldrich. Water was purified with a Millipore Direct-Q system with a final resistance of 18.2 M ohm. HOPG was obtained from SPI Supplies.

Synthesis of Cu and Au Nanoparticles. The synthesis of decanethiolate (DT)-capped Au nanoparticles followed the modified two-phase reduction method.[12,45,46] The synthesis of decanethiolate-capped Cu nanoclusters was described.[12,47] Briefly, $CuCl_2$ was dissolved in water in the presence of 4.3 M KBr. Cu^{2+} was converted to $CuBr_4^{2-}$, which was transferred from aqueous phase to the organic phase by adding a solution of TOABr in toluene (40 mL toluene, 180 mM TOABr). After 20 min of vigorous stirring, the aqueous solution was removed. The toluene solution was stirred under an argon purge to eliminate oxygen from the system. 0.36 mL of decanethiol was added, and the solution was stirred for another 1 h, resulting in the color change of the solution from dark purple to light green. $NaBH_4$ solution (25 mL, 0.4 M) was added dropwise. After reaction for 2 h under argon, the aqueous layer was removed and the solution was stirred overnight.

Synthesis of AuCu Alloy Nanoparticles from Mixed Cu- and Au-Precursor Nanoparticles. The solutions of the as-synthesized Au nanoparticles and Cu nanoclusters were mixed in a controlled ratio.[12] The mixed solution was then concentrated by a factor of ∼15 in a glass reactor and was kept in an oven under controlled temperature (150−170 °C) and reaction time. 156 °C was identified as an optimal temperature for forming nanocubes by examining a series of temperatures ranging from 150 to 172 °C.

AP-XPS Experiments. Most AP-XPS experiments were performed at the IOS beamline of National Synchrotron Light Source II (NSLS-II), Brookhaven National Laboratory. CO oxidation over the $Cu_{50}Au_{50}$ nanoparticles, loaded on Al_2O_3 and supported on HOPG, was performed using a laboratory-based AP-XPS system located at the Center for Functional Materials (CFN), Brookhaven National Laboratory.[48] The AP-XPS instrument is equipped with a reaction chamber with the base pressure <5 × 10^{-9} Torr, a SPECS Phoibos NAP150 hemispherical analyzer, and a sputtering gun for surface preparation. The multiple differential pumping stages between the reaction chamber and the hemispherical analyzer create a pressure difference by maintaining ultrahigh vacuum conditions (lower than 1 × 10^{-7} Torr) in the analyzer, while the pressure in the reaction chamber is a few Torr. Photoemitted electrons leave the high-pressure reaction chamber through a small cone-shaped aperture into the differentially pumped transfer lenses system toward the electron energy analyzer, thereby allowing for continuously acquiring XPS spectra at pressures of up to ∼5 Torr in the reaction chamber. The photon energy used was 650 eV for O 1s, C 1s, and 1150 eV for Cu 2p core levels and Cu LMM relevant for the present work. For the laboratory-based AP-XPS system, a monochromatized, focused Al Kα X-ray source (hn = 1486.6 eV) is used for acquiring the XPS spectra. All the spectra were acquired at the emission angle of 70° between the sample surface normal and the electron analyzer optic axis of the XPS spectrometer. XPS spectra were analyzed using a Shirley-type background with the Gaussian/Lorentz sum formula and the Voigt function, and binding energies in each spectrum were corrected by referring to the Fermi level.

TEM. HAADF-STEM observations of the HOPG-supported $Cu_{50}Au_{50}$ NPs were performed with an FEI Talos F200X microscopy operated at 200 kV.

Density Functional Theory (DFT) Modeling. Periodic DFT calculations were performed using the Vienna Ab initio Simulation Package (VASP).[49,50] Perdew, Burke, and Ernzerhof (PBE) generalized gradient approximation (GGA) and the projector augmented-wave (PAW) potentials were used to describe the electron−electron exchange and core−electron potential separately.[51] The plane-wave cutoff energy was set to be 500 eV. The Brillouin-zone integration was performed using (4 × 4 × 1) K-point meshes based on Monkhorst−Pack grids.[52] Our calculated lattice parameters for Cu, Au, and Cu_3Au slabs are 3.64 4.14, and 3.9 Å. We modeled the dissociation pathway and associated energy barrier by using the nudged elastic band (NEB) method with 5 intermediate images between the initial state and the final state.[53]

The adsorption energy of O_2 was calculated using

$$E_{ads} = E_{slab}^{tot} - E_S - \frac{N}{2}E_{O_2}$$

where E_{slab}^{tot} is the total energy of the whole system with one H atom (or H_2 molecule), E_S is the free energy of the slab without adsorbed O, E_{O_2} is the energy of an isolated O_2 molecule, and N is the number of O newly adsorbed into the system, which is equal to 1 throughout the whole work.

The surface energy γ of a slab was calculated as

$$\gamma = \frac{E_S - nE_B}{2A}$$

where n is the total number of atoms in the slab, E_B is the energy per atom in the bulk crystal, and A is the area of the top or bottom surface of the slab. The cleavage energy is twice the surface energy.

The adhesion energy W was calculated following

$$E_{1-2} = \frac{E_1 + E_2 - E_{12}}{A}$$

where E_1, E_2, and E_{12} are the energies of slab 1, slab 2, and the slab 1−2 system, respectively; A is the slab 1−2 interface area. The slabs 1 and 2 are composed of 4 atomic layers in this work. The graphite slab was unstrained with a lattice parameter of

https://doi.org/10.1021/acscatal.3c06171
ACS Catal. 2024, 14, 5662−5674

2.46 Å. For Cu-graphite, we used a 1 × 1 supercell. The lattice parameter of bulk Cu slab is $3.64/\sqrt{2}$=2.57 Å. The natural lattice misfit between the Cu slab and graphite is ∼−4%. For the Au-graphite system, we used a 6 × 7 supercell. The natural lattice misfit between the Au slab and graphite is ∼−3%.

■ ASSOCIATED CONTENT

Supporting Information

The Supporting Information is available free of charge at https://pubs.acs.org/doi/10.1021/acscatal.3c06171.

Additional data including HRTEM images showing electron beam-induced damage to the encapsulation layer and minimum reaction energy for the dissociation adsorption of molecular O_2 on Cu(111) (PDF)

Supplementary in situ TEM video 1: embedment of Cu NPs into the HOPG support under UHV annealing at 200 °C (AVI)

Supplementary in situ TEM video 2: encapsulation of a $Cu_{50}Au_{50}$ NP loaded on HOPG at 200 °C and 1 × 10^{-3} Torr of O_2 gas flow (MP4)

Supplementary in situ TEM video 3: electron beam-induced damage to the encapsulation of a $Cu_{50}Au_{50}$ NP loaded on the graphite support at 200 °C and 1 × 10^{-3} Torr of O_2 gas flow (AVI)

■ AUTHOR INFORMATION

Corresponding Author

Guangwen Zhou − *Department of Mechanical Engineering and Materials Science and Engineering Program, State University of New York at Binghamton, Binghamton, New York 13902, United States;* orcid.org/0000-0002-9243-293X; Email: gzhou@binghamton.edu

Authors

Jianyu Wang − *Department of Mechanical Engineering and Materials Science and Engineering Program, State University of New York at Binghamton, Binghamton, New York 13902, United States*

Xiaobo Chen − *Department of Mechanical Engineering and Materials Science and Engineering Program, State University of New York at Binghamton, Binghamton, New York 13902, United States*

Chaoran Li − *Department of Mechanical Engineering and Materials Science and Engineering Program, State University of New York at Binghamton, Binghamton, New York 13902, United States*

Yaguang Zhu − *Department of Mechanical Engineering and Materials Science and Engineering Program, State University of New York at Binghamton, Binghamton, New York 13902, United States*

Jing Li − *Materials Science and Engineering Program, State University of New York at Binghamton, Binghamton, New York 13902, United States; Department of Chemistry, State University of New York at Binghamton, Binghamton, New York 13902, United States*

Shiyao Shan − *Materials Science and Engineering Program, State University of New York at Binghamton, Binghamton, New York 13902, United States; Department of Chemistry, State University of New York at Binghamton, Binghamton, New York 13902, United States;* orcid.org/0000-0001-9240-7227

Adrian Hunt − *National Synchrotron Light Source II, Brookhaven National Laboratory, Upton, New York 11973, United States;* orcid.org/0000-0002-5283-9647

Iradwikanari Waluyo − *National Synchrotron Light Source II, Brookhaven National Laboratory, Upton, New York 11973, United States;* orcid.org/0000-0002-4046-9722

J. Anibal Boscoboinik − *Center for Functional Nanomaterials, Brookhaven National Laboratory, Upton, New York 11973, United States;* orcid.org/0000-0002-5090-7079

Chuan-Jian Zhong − *Materials Science and Engineering Program, State University of New York at Binghamton, Binghamton, New York 13902, United States; Department of Chemistry, State University of New York at Binghamton, Binghamton, New York 13902, United States;* orcid.org/0000-0003-0746-250X

Complete contact information is available at: https://pubs.acs.org/10.1021/acscatal.3c06171

Notes

The authors declare no competing financial interest.

■ ACKNOWLEDGMENTS

This work was supported by the U.S. Department of Energy (DOE), Office of Basic Energy Sciences, Division of Materials Sciences and Engineering under Award No. DE-SC0001135. The work on the synthesis and preparation of the nanoparticles and catalysts was supported by the National Science Foundation (CHE 2102482). This research used the 23-ID-2 (IOS) beamline at the National Synchrotron Light Source II, the Proximal Probes and Electron Microcopy Facilities and the Theory and Computation resources of the Center for Functional Nanomaterials, which are U.S. DOE Office of Science User Facilities, at Brookhaven National Laboratory under Contract No. DE-SC0012704.

■ REFERENCES

(1) Ivanova, S.; Petit, C.; Pitchon, V. A New Preparation Method for the Formation of Gold Nanoparticles on an Oxide Support. *Appl. Catal., A* **2004**, *267* (1), 191−201.

(2) Kitsudo, Y.; Iwamoto, A.; Matsumoto, H.; Mitsuhara, K.; Nishimura, T.; Takizawa, M.; Akita, T.; Maeda, Y.; Kido, Y. Final State Effect for Au 4f Line from Gold-Nano-Particles Grown on Oxides and HOPG Supports. *Surf. Sci.* **2009**, *603* (13), 2108−2114.

(3) Matsubu, J. C.; Zhang, S.; DeRita, L.; Marinkovic, N. S.; Chen, J. G.; Graham, G. W.; Pan, X.; Christopher, P. Adsorbate-Mediated Strong Metal−Support Interactions in Oxide-Supported Rh Catalysts. *Nat. Chem.* **2017**, *9* (2), 120−127.

(4) Luo, Z.; Zhao, G.; Pan, H.; Sun, W. Strong Metal−Support Interaction in Heterogeneous Catalysts. *Adv. Energy Mater.* **2022**, *12* (37), 2201395.

(5) Wang, H.; Wang, L.; Xiao, F.-S. New Routes for the Construction of Strong Metal—Support Interactions. *Sci. China: Chem.* **2022**, *65* (11), 2051−2057.

(6) Pu, T.; Zhang, W.; Zhu, M. Engineering Heterogeneous Catalysis with Strong Metal−Support Interactions: Characterization, Theory and Manipulation. *Angew. Chem., Int. Ed.* **2023**, *62* (4), No. e202212278.

(7) Tang, H.; Wei, J.; Liu, F.; Qiao, B.; Pan, X.; Li, L.; Liu, J.; Wang, J.; Zhang, T. Strong Metal−Support Interactions between Gold Nanoparticles and Nonoxides. *J. Am. Chem. Soc.* **2016**, *138* (1), 56−59.

(8) Zhang, S.; Plessow, P. N.; Willis, J. J.; Dai, S.; Xu, M.; Graham, G. W.; Cargnello, M.; Abild-Pedersen, F.; Pan, X. Dynamical Observation and Detailed Description of Catalysts under Strong Metal−Support Interaction. *Nano Lett.* **2016**, *16* (7), 4528−4534.

(9) Datye, A. K.; Kalakkad, D. S.; Yao, M. H.; Smith, D. J. Comparison of Metal-Support Interactions in Pt/TiO_2 and Pt/CeO_2. *J. Catal.* **1995**, *155* (1), 148−153.
(10) Dulub, O.; Hebenstreit, W.; Diebold, U. Imaging Cluster Surfaces with Atomic Resolution: The Strong Metal-Support Interaction State of Pt Supported on TiO_2(110). *Phys. Rev. Lett.* **2000**, *84* (16), 3646−3649.
(11) Yin, P.; Shen, S.-C.; Zhang, L.-L.; Zheng, X.-S.; Zuo, M.; Ding, Y.-W.; Liang, H.-W. Ultra-High-Temperature Strong Metal-Support Interactions in Carbon-Supported Catalysts. *Cell Rep. Phys. Sci.* **2022**, *3* (8), 100984.
(12) Yin, J.; Shan, S.; Yang, L.; Mott, D.; Malis, O.; Petkov, V.; Cai, F.; Shan Ng, M.; Luo, J.; Chen, B. H.; Engelhard, M.; Zhong, C.-J. Gold−Copper Nanoparticles: Nanostructural Evolution and Bifunctional Catalytic Sites. *Chem. Mater.* **2012**, *24* (24), 4662−4674.
(13) Bauer, J. C.; Mullins, D.; Li, M.; Wu, Z.; Payzant, E. A.; Overbury, S. H.; Dai, S. Synthesis of Silica Supported AuCu Nanoparticle Catalysts and the Effects of Pretreatment Conditions for the CO Oxidation Reaction. *Phys. Chem. Chem. Phys.* **2011**, *13* (7), 2571−2581.
(14) Andrews, E.; Fang, Y.; Flake, J. Electrochemical Reduction of CO_2 at CuAu Nanoparticles: Size and Alloy Effects. *J. Appl. Electrochem.* **2018**, *48* (4), 435−441.
(15) Guan, Y.; Liu, Y.; Ren, Q.; Dong, Z.; Luo, L. Oxidation-Induced Phase Separation of Carbon-Supported CuAu Nanoparticles for Electrochemical Reduction of CO_2. *Nano Res.* **2023**, *16* (2), 2119−2125.
(16) Chinchen, G. C.; Waugh, K. C.; Whan, D. A. The Activity and State of the Copper Surface in Methanol Synthesis Catalysts. *Appl. Catal.* **1986**, *25* (1), 101−107.
(17) Lin, F.; Jiang, X.; Boreriboon, N.; Wang, Z.; Song, C.; Cen, K. Effects of Supports on Bimetallic Pd-Cu Catalysts for CO_2 Hydrogenation to Methanol. *Appl. Catal., A* **2019**, *585*, 117210.
(18) Moharreri, E.; Jafari, T.; Rathnayake, D.; Khanna, H.; Kuo, C.-H.; Suib, S. L.; Nandi, P. Role of Catalytic Nitrile Decomposition in Tricopper Complex Mediated Direct Partial Oxidation of Methane to Methanol. *Sci. Rep.* **2021**, *11* (1), 19175.
(19) Rodriguez, J. A.; Liu, P.; Hrbek, J.; Evans, J.; Pérez, M. Water Gas Shift Reaction on Cu and Au Nanoparticles Supported on CeO2(111) and ZnO(0001): Intrinsic Activity and Importance of Support Interactions. *Angew. Chem., Int. Ed.* **2007**, *46* (8), 1329−1332.
(20) Dong, Z.; Nian, Y.; Liu, H.; Chen, J.; Wang, Y.; Wang, S.; Xu, J.; Han, Y.; Luo, L. Revealing Synergetic Structural Activation of a CuAu Surface during Water−Gas Shift Reaction. *Proc. Natl. Acad. Sci. U. S. A.* **2022**, *119* (23), No. e2120088119.
(21) Petkov, V.; Ren, Y.; Shan, S.; Luo, J.; Zhong, C.-J. A Distinct Atomic Structure−Catalytic Activity Relationship in 3−10 Nm Supported Au Particles. *Nanoscale* **2014**, *6* (1), 532−538.
(22) Mukundan, V.; Shan, S.; Zhong, C.-J.; Malis, O. Effect of Chemical Composition on the Nanoscale Ordering Transformations of Physical Mixtures of Pd and Cu Nanoparticles. *J. Nanomater.* **2018**, *2018*, No. e9087320.
(23) Ferrah, D.; Haines, A. R.; Galhenage, R. P.; Bruce, J. P.; Babore, A. D.; Hunt, A.; Waluyo, I.; Hemminger, J. C. Wet Chemical Growth and Thermocatalytic Activity of Cu-Based Nanoparticles Supported on TiO_2 Nanoparticles/HOPG: In Situ Ambient Pressure XPS Study of the CO_2 Hydrogenation Reaction. *ACS Catal.* **2019**, *9* (8), 6783−6802.
(24) Huang, Y.; Tang, J.; Gai, L.; Gong, Y.; Guan, H.; He, R.; Lyu, H. Different Approaches for Preparing a Novel Thiol-Functionalized Graphene Oxide/Fe-Mn and Its Application for Aqueous Methylmercury Removal. *Chem. Eng. J.* **2017**, *319*, 229−239.
(25) Favaro, M.; Agnoli, S.; Perini, L.; Durante, C.; Gennaro, A.; Granozzi, G. Palladium Nanoparticles Supported on Nitrogen-Doped HOPG: A Surface Science and Electrochemical Study. *Phys. Chem. Chem. Phys.* **2013**, *15* (8), 2923−2931.
(26) Rousseau, B.; Estrade-Szwarckopf, H.; Thomann, A.-L.; Brault, P. Stable C-Atom Displacements on HOPG Surface under Plasma Low-Energy Argon-Ion Bombardment. *Appl. Phys. A: Mater. Sci. Process.* **2003**, *77* (3), 591−597.
(27) Sivaranjini, B.; Mangaiyarkarasi, R.; Ganesh, V.; Umadevi, S. Vertical Alignment of Liquid Crystals Over a Functionalized Flexible Substrate. *Sci. Rep.* **2018**, *8* (1), 8891.
(28) Díez, N.; Śliwak, A.; Gryglewicz, S.; Grzyb, B.; Gryglewicz, G. Enhanced Reduction of Graphene Oxide by High-Pressure Hydrothermal Treatment. *RSC Adv.* **2015**, *5* (100), 81831−81837.
(29) Wang, J.; Li, C.; Zhu, Y.; Boscoboinik, J. A.; Zhou, G. Insight into the Phase Transformation Pathways of Copper Oxidation: From Oxygen Chemisorption on the Clean Surface to Multilayer Bulk Oxide Growth. *J. Phys. Chem. C* **2018**, *122* (46), 26519−26527.
(30) Murphy, S.; Nielsen, R. M.; Strebel, C.; Johansson, M.; Nielsen, J. H. Catalytic Oxidation of Graphite by Mass-Selected Ruthenium Nanoparticles. *Carbon* **2011**, *49* (2), 376−385.
(31) Yoon, B.; Luedtke, W. D.; Gao, J.; Landman, U. Diffusion of Gold Clusters on Defective Graphite Surfaces. *J. Phys. Chem. B* **2003**, *107* (24), 5882−5891.
(32) Yang, D.; Velamakanni, A.; Bozoklu, G.; Park, S.; Stoller, M.; Piner, R. D.; Stankovich, S.; Jung, I.; Field, D. A.; Ventrice, C. A.; Ruoff, R. S. Chemical Analysis of Graphene Oxide Films after Heat and Chemical Treatments by X-Ray Photoelectron and Micro-Raman Spectroscopy. *Carbon* **2009**, *47* (1), 145−152.
(33) Rani, J. R.; Lim, J.; Oh, J.; Kim, D.; Lee, D.; Kim, J.-W.; Shin, H. S.; Kim, J. H.; Jun, S. C. Substrate and Buffer Layer Effect on the Structural and Optical Properties of Graphene Oxide Thin Films. *RSC Adv.* **2013**, *3* (17), 5926−5936.
(34) Sengupta, I.; Chakraborty, S.; Talukdar, M.; Pal, S. K.; Chakraborty, S. Thermal Reduction of Graphene Oxide: How Temperature Influences Purity. *J. Mater. Res.* **2018**, *33* (23), 4113−4122.
(35) Zhu, Y.; Wang, J.; Patel, S. B.; Li, C.; Head, A. R.; Boscoboinik, J. A.; Zhou, G. Tuning the Surface Reactivity of Oxides by Peroxide Species. *Proc. Natl. Acad. Sci. U. S. A.* **2023**, *120* (13), No. e2215189120.
(36) Li, C.; Zhang, P.; Wang, J.; Boscoboinik, J. A.; Zhou, G. Tuning the Deoxygenation of Bulk-Dissolved Oxygen in Copper. *J. Phys. Chem. C* **2018**, *122* (15), 8254−8261.
(37) Wang, J.; Lu, D.; Li, C.; Zhu, Y.; Boscoboinik, J. A.; Zhou, G. Measuring Charge Transfer between Adsorbate and Metal Surfaces. *J. Phys. Chem. Lett.* **2020**, *11* (16), 6827−6834.
(38) Wang, J.; Li, C.; Zhu, Y.; Boscoboinik, J. A.; Zhou, G. In Situ Monitoring of H_2-Induced Nonstoichiometry in Cu_2O. *J. Phys. Chem. Lett.* **2022**, *13* (24), 5597−5604.
(39) Jeong, H.-K.; Lee, Y. P.; Lahaye, R. J. W. E.; Park, M.-H.; An, K. H.; Kim, I. J.; Yang, C.-W.; Park, C. Y.; Ruoff, R. S.; Lee, Y. H. Evidence of Graphitic AB Stacking Order of Graphite Oxides. *J. Am. Chem. Soc.* **2008**, *130* (4), 1362−1366.
(40) Okazaki-Maeda, K.; Kohyama, M. Atomic Oxygen Adsorption on Au(100) and Au(111): Effects of Coverage. *Chem. Phys. Lett.* **2010**, *492* (4), 266−271.
(41) Li, C.; Liu, Q.; Boscoboinik, J. A.; Zhou, G. Tuning the Surface Composition of Cu_3Au Binary Alloy. *Phys. Chem. Chem. Phys.* **2020**, *22* (6), 3379−3389.
(42) Szabo, T.; Maroni, P.; Szilagyi, I. Size-Dependent Aggregation of Graphene Oxide. *Carbon* **2020**, *160*, 145−155.
(43) Lu, K.-Q.; Li, Y.-H.; Tang, Z.-R.; Xu, Y.-J. Roles of Graphene Oxide in Heterogeneous Photocatalysis. *ACS Mater. Au* **2021**, *1* (1), 37−54.
(44) Lykhach, Y.; Kozlov, S. M.; Skála, T.; Tovt, A.; Stetsovych, V.; Tsud, N.; Dvořák, F.; Johánek, V.; Neitzel, A.; Mysliveček, J.; Fabris, S.; Matolín, V.; Neyman, K. M.; Libuda, J. Counting Electrons on Supported Nanoparticles. *Nat. Mater.* **2016**, *15* (3), 284−288.
(45) Brust, M.; Walker, M.; Bethell, D.; Schiffrin, D. J.; Whyman, R. Synthesis of Thiol-Derivatised Gold Nanoparticles in a Two-Phase Liquid−Liquid System. *J. Chem. Soc., Chem. Commun.* **1994**, *0* (7), 801−802.
(46) Hostetler, M. J.; Zhong, C.-J.; Yen, B. K. H.; Anderegg, J.; Gross, S. M.; Evans, N. D.; Porter, M.; Murray, R. W. S. Monolayer-

https://doi.org/10.1021/acscatal.3c06171
ACS Catal. 2024, 14, 5662−5674

Protected Metal Alloy Clusters. *J. Am. Chem. Soc.* **1998**, *120* (36), 9396−9397.
(47) Mott, D.; Galkowski, J.; Wang, L.; Luo, J.; Zhong, C.-J. Synthesis of Size-Controlled and Shaped Copper Nanoparticles. *Langmuir* **2007**, *23* (10), 5740−5745.
(48) Eads, C. N.; Zhong, J.-Q.; Kim, D.; Akter, N.; Chen, Z.; Norton, A. M.; Lee, V.; Kelber, J. A.; Tsapatsis, M.; Boscoboinik, J. A.; Sadowski, J. T.; Zahl, P.; Tong, X.; Stacchiola, D. J.; Head, A. R.; Tenney, S. A. Multi-Modal Surface Analysis of Porous Films under Operando Conditions. *AIP Adv.* **2020**, *10* (8), 085109.
(49) Kresse, G.; Furthmüller, J. Efficient Iterative Schemes for Ab Initio Total-Energy Calculations Using a Plane-Wave Basis Set. *Phys. Rev. B* **1996**, *54* (16), 11169−11186.
(50) Kresse, G.; Furthmüller, J. Efficiency of Ab-Initio Total Energy Calculations for Metals and Semiconductors Using a Plane-Wave Basis Set. *Comput. Mater. Sci.* **1996**, *6* (1), 15−50.
(51) Perdew, J. P.; Burke, K.; Ernzerhof, M. Generalized Gradient Approximation Made Simple. *Phys. Rev. Lett.* **1996**, *77* (18), 3865−3868.
(52) Monkhorst, H. J.; Pack, J. D. Special Points for Brillouin-Zone Integrations. *Phys. Rev. B* **1976**, *13* (12), 5188−5192.
(53) Henkelman, G.; Uberuaga, B. P.; Jónsson, H. A Climbing Image Nudged Elastic Band Method for Finding Saddle Points and Minimum Energy Paths. *J. Chem. Phys.* **2000**, *113* (22), 9901−9904.

https://doi.org/10.1021/acscatal.3c06171
ACS Catal. 2024, 14, 5662−5674